THE JOURNAL OF PHYSICAL CHEMISTRY B

Article

pubs.acs.org/JPCB

Glutamine and Asparagine Side Chain Hyperconjugation-Induced Structurally Sensitive Vibrations

David Punihaole, Zhenmin Hong, Ryan S. Jakubek, Elizabeth M. Dahlburg, Steven Geib, and Sanford A. Asher*

Department of Chemistry, University of Pittsburgh, 219 Parkman Avenue, Chevron Science Center, Pittsburgh, Pennsylvania 15260, United States

Supporting Information

ABSTRACT: We identified vibrational spectral marker bands that sensitively report on the side chain structures of glutamine (Gln) and asparagine (Asn). Density functional theory (DFT) calculations indicate that the Amide III^P (AmIII^P) vibrations of Gln and Asn depend cosinusoidally on their side chain OCCC dihedral angles (the χ_3 and χ_2 angles of Gln and Asn, respectively). We use UV resonance Raman (UVRR) and visible Raman spectroscopy to experimentally correlate the AmIII^P Raman band frequency to the primary amide OCCC dihedral angle. The AmIII^P structural sensitivity derives from the Gln (Asn) C_β−C_γ (C_α−C_β) stretching component of the vibration. The C_β−C_γ (C_α−C_β) bond length inversely correlates with the AmIII^P band frequency. As the C_β−C_γ (C_α−C_β) bond length decreases, its stretching force constant increases, which results in an upshift in the AmIII^P frequency. The C_β−C_γ (C_α−C_β) bond length dependence on the χ_3 (χ_2) dihedral angle results from hyperconjugation between the C_δ═O_ϵ (C_γ═O_δ) π^* and C_β−C_γ (C_α−C_β) σ orbitals. Using a Protein Data Bank library, we show that the χ_3 and χ_2 dihedral angles of Gln and Asn depend on the peptide backbone Ramachandran angles. We demonstrate that the inhomogeneously broadened AmIII^P band line shapes can be used to calculate the χ_3 and χ_2 angle distributions of peptides. The spectral correlations determined in this study enable important new insights into protein structure in solution, and in Gln- and Asn-rich amyloid-like fibrils and prions.

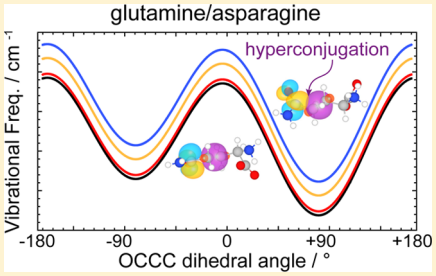

INTRODUCTION

Amyloid-like fibril protein aggregates and prion proteins often contain stretches of glutamine (Gln) and asparagine (Asn) residues. For example, polyglutamine (polyGln)-rich fibrils are the pathological hallmarks of several "CAG" codon repeat diseases.[1−9] Similarly, Sup35p and Ure2p prions contain Gln- and Asn-rich regions that drive their aggregation and cause loss-of-function of these normally soluble proteins.[10]

Because Gln and Asn side chains can hydrogen bond to water, the peptide backbone, or other side chains, they serve unique roles in protein structure and conformational transitions. Unfortunately, there is relatively little known about the mechanisms by which the primary amide groups of Gln and Asn interact with other protein constituents or what role they play in the aggregation of prions and fibrils. Consequently, it is important to find spectroscopic markers that can be used to monitor the conformations and hydrogen bonding environments of Asn and Gln side chains in order to develop a deeper understanding of the roles that these residues play in protein aggregation.

There are few methods to quantitatively examine the conformations of Gln and Asn side chains in prion and fibril aggregates. Recent solid-state NMR studies[11−13] suggest that there are at least two different populations of Gln side chain conformers in polyGln fibrils. Sharma et al.[14] claim on the basis of low-resolution X-ray fiber and powder diffraction data that the side chains in polyGln fibrils adopt an unusual bent conformation; however, these highly uncommon side chain structures have not been substantiated by other studies.

High resolution X-ray diffraction studies[15,16] on small peptide microcrystals that contain amyloidogenic sequences have revealed important, atomic-resolution details regarding the steric zipper interactions that could occur in Gln- and Asn-rich prions and fibrils. These studies indicate, for example, that differences in the structures and hydrogen bonding interactions of amino acid side chains give rise to different fibril polymorphs. However, the conformations observed in the small peptide crystals may not reflect the side chain structures and hydrogen bonding interactions that occur in bona fide prion and fibril aggregates.

UV resonance Raman (UVRR) is a powerful, emerging tool for studying the conformations of proteins, as well as the structure, local hydrogen bonding, and dielectric environments of amino acid side chains.[17−28] Deep UV excitation (∼200 nm) selectively resonance enhances secondary and primary amide vibrations.[29,30] Previous investigations of secondary amide vibrations have developed a detailed understanding of the UVRR spectral dependence on the peptide bond structure and its hydrogen bonding.[31−34] For example, Asher and co-workers[35−37] quantitatively correlated the Amide III$_3$

Received: August 6, 2015
Revised: September 17, 2015
Published: September 21, 2015

ACS Publications © 2015 American Chemical Society

DOI: 10.1021/acs.jpcb.5b07651
J. Phys. Chem. B 2015, 119, 13039−13051

($AmIII_3$) frequency to the peptide bond Ramachandran Ψ dihedral angle. They determined that the structural sensitivity of the $AmIII_3$ vibration derives from coupling between the peptide backbone amide N−H and C_α−H bending motions.[35] This fundamental insight enabled incisive investigations that elucidated, in detail, the mechanism of α-helix (un)folding in a wide range of solution environments.[38−43]

We seek to develop a similar deep understanding of the UVRR spectral dependence of primary amide vibrations on the structure of Gln and Asn side chains. In this work, we discover the structural sensitivity of the Amide III^P ($AmIII^P$) vibration on the primary amide OCCC dihedral angle (the χ_3 and χ_2 angles of the side chains Gln and Asn, respectively). The potential energy distribution (PED) of this vibration in Gln (Asn) contains significant contributions of C_β−C_γ (C_α−C_β) stretching, $N_\epsilon H_2$ ($N_\delta H_2$) rocking, and C_δ−N_ϵ (C_γ−N_δ) stretching motions. We find that the structural sensitivity of the $AmIII^P$ mode originates mainly from the C_β−C_γ (C_α−C_β) bond length dependence on the χ_3 (χ_2) dihedral angle. We demonstrate that the C_β−C_γ (C_α−C_β) bond length correlation on the χ_3 (χ_2) dihedral angle derives from hyperconjugation between the C_β−C_γ (C_α−C_β) σ orbital and the C_δ=O_ϵ (C_γ=O_δ) π* orbital.

We compare our results with the Gln and Asn entries of the Shapovalov and Dunbrack side chain rotamer library[44] and examine the dependence of Gln (Asn) χ_3 (χ_2) dihedral angles on the peptide backbone Ramachandran (Φ, Ψ) angles. We observe distinct χ_3 and χ_2 dihedral angle preferences for Gln and Asn residues that adopt PPII, β-sheet and α-helix Ramachandran angles. Applying this new insight and the dependence of the χ_3 dihedral angle on the $AmIII^P$ vibrational frequency, we determine the χ_3 angle distribution of Gln_3 and Asp_2-Gln_{10}-Lys_2 peptides in aqueous solution. We find that Gln_3 and Asp_2-Gln_{10}-Lys_2 favor χ_3 dihedral angles similar to those of Gln in solution. This result is consistent with Gln_3 and Asp_2-Gln_{10}-Lys_2 containing side chains that are completely solvated.

Our work here develops a novel spectral marker for experimentally probing the structures of Asn and Gln side chains in fibrils and prion aggregates. Our methodology does not require extensive isotopic labeling or crystallization and allows us to monitor the side chain structural changes that occur during protein aggregation. This enables crucial, molecular-level insights into the role that Gln and Asn side chains play in stabilizing fibril and prion aggregates. We are developing new insights into why Gln- and Asn-rich sequences have strong propensities to aggregate into amyloid-like fibrils and prions.

■ EXPERIMENTAL DETAILS

Materials. L-Glutamine (L-Gln, ≥99% purity), L-glutamine *t*-butyl ester hydrochloride (Gln-TBE, ≥98% purity), and glycyl-L-glutamine (Gly-Gln, ≥97% purity) were purchased from Sigma-Aldrich. D-Glutamine (D-Gln, 98% purity) was purchased from Acros Organics, and *N*-Acetyl-L-glutamine (NAcGln, 97% purity) was purchased from Spectrum Chemical Mfg. Corp. L-seryl-L-asparagine (Ser-Asn, ≥99% purity) was purchased from Bachem. Optima-grade H_2O was purchased from Fisher Scientific, and D_2O (99.9% atom D purity) was purchased from Cambridge Isotope Laboratories, Inc. Gln_3 was purchased from Pierce Biotechnology at 95% purity.

Sample Preparation. Gly-Gln and Ser-Asn were obtained as crystalline powders and used without further purification or recrystallization. D-Gln, NAcGln, L-Asn, and GlnTBE crystals were prepared by drying saturated solutions in water. L-Gln crystals were obtained by drying a saturated solution in the presence of 0.1 M NaCl. N-deuterated crystals were prepared via multiple rounds of recrystallization in D_2O. Samples of Gln_3 were prepared at 0.5 mg·mL^{-1} in HPLC-grade water containing 0.05 M sodium perchlorate (Sigma-Aldrich, ≥98% purity). The sodium perchlorate was used as an internal intensity standard to allow us to subtract the contribution of water.

X-ray Diffraction. X-ray diffraction of crystals was performed using a Bruker X8 Prospector Ultra equipped with a copper microfocus tube (λ = 1.54178 Å). The crystals were mounted and placed in a cold stream of N_2 gas (230 K) for data collection. The frames collected on each crystal specimen were integrated with the Bruker SAINT software package using the narrow-frame algorithm. The Supporting Information discusses, in detail, the methods used to determine the unit cells and crystal structures of the compounds examined.

Visible Raman Spectroscopy. Visible excitation Raman spectra of crystals were collected using a Renishaw inVia spectrometer equipped with a research-grade Leica microscope. Spectra were collected using the 633 nm excitation line from a HeNe laser and a 5× objective lens. The spectrometer resolution was ∼2 cm^{-1}. The 918 and 1376 cm^{-1} bands of acetonitrile[45] were used to calibrate the spectral frequencies.

UV Resonance Raman Spectroscopy. UV resonance Raman (UVRR) spectra of crystals were collected using CW 229 nm light generated by an Innova 300C FreD frequency doubled Ar^+ laser.[46] The crystalline specimens were spun in a cylindrical brass cell to prevent the accumulation of thermal or photodegradation products. A SPEX triplemate spectrograph, modified for use in the deep UV, was utilized to disperse the Raman scattered light. A Spec-10 CCD camera (Princeton Instruments, model 735-0001) with a Lumagen-E coating was used to detect the Raman light. The power of UV light illuminating the sample ranged from ∼1.5 to 2 mW. The 801, 1028, 2852, and the 2938 cm^{-1} bands of cyclohexane were used to calibrate the 229 nm excitation UVRR spectral frequencies.

UVRR solution-state measurements were made using ∼204 nm excitation. The UV light was generated by Raman shifting the third harmonic of a Nd:YAG laser (Coherent, Inc.) with H_2 gas (∼30 psi) and selecting the fifth anti-Stokes line. A thermostated (20°) flow cell was employed to circulate solutions in order to prevent the contribution of photodegradation products. The scattered light was dispersed and imaged using a double monochromator, modified for use in the UV in a subtractive configuration[47] and detected with a Spec-10 CCD camera.

■ COMPUTATIONAL DETAILS

Density Functional Theory (DFT) Calculations. The DFT calculations[48] were carried out using the GAUSSIAN 09 package.[49] The geometry optimizations and frequency calculations were performed using the M06-2X functional[50] and the 6-311++g** basis set. The presence of water was simulated implicitly by employing a polarizable continuum dielectric model (PCM). Vibrational frequencies were calculated using the harmonic approximation. The calculated frequencies were not scaled. The potential energy distribution (PED) of each vibration was obtained from the Gaussian output files by employing a MATLAB program that we wrote (see Supporting Information). Figure 1 shows the DFT calculated minimum energy structure of L-Gln and the atomic

DOI: 10.1021/acs.jpcb.5b07651
J. Phys. Chem. B 2015, 119, 13039−13051

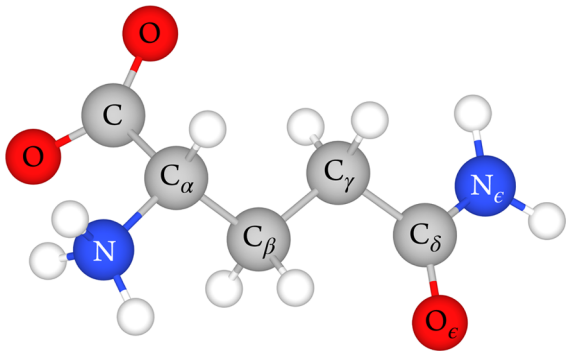

Figure 1. Geometry of optimized structure and atomic labeling scheme of L-Gln used in DFT calculations and band assignments.

labeling scheme. To study the conformational dependence of the Raman bands, we fixed the χ_3 dihedral angle of L-Gln, reoptimized the geometry, and calculated the harmonic vibrational frequencies for a series of conformers with χ_3 angles of −16°, 0°, 4°, ±30°, ±60°, ±90°, ±120°, ±150°, and ±180°.

■ RESULTS AND DISCUSSION

Assignment of L-Gln UVRR Bands in H_2O and D_2O. Figure 2 shows the band-resolved ∼204 nm excitation UVRR spectra of L-Gln in H_2O and D_2O. Visible Raman and infrared spectra band assignments of L-Gln were reported previously by Ramirez and co-workers for both solid-state crystalline samples[51] and in the solution state.[52] Ramirez and co-workers made assignments without performing normal mode calculations in their study of crystalline L-Gln. In their solution-state study, they employed DFT calculations to aid in band assignments. We found that their reported frequencies did not match those in our solution-state UVRR spectra and that their band assignments were inconsistent with our intensity expectations of the resonance enhanced bands.

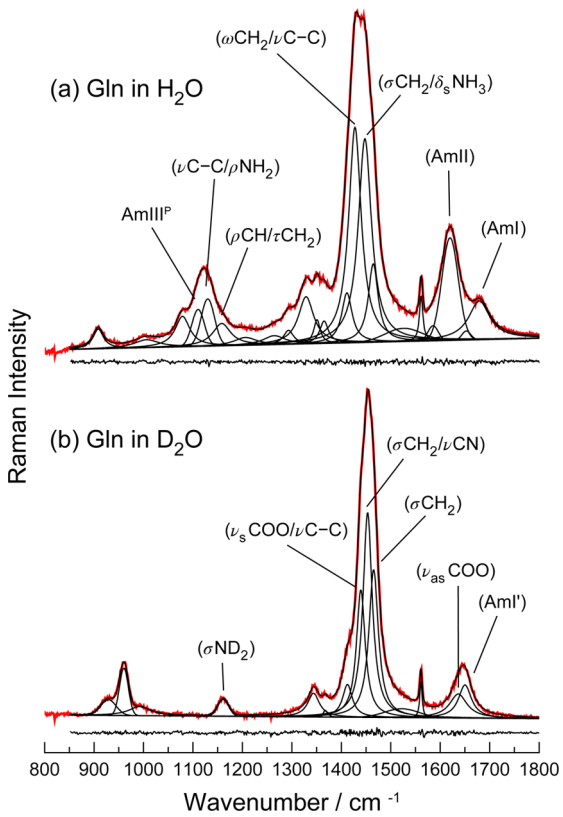

Figure 2. UVRR spectra excited at ∼204 nm of L-Gln in (a) H_2O and (b) D_2O. The spectral contributions of the solvents have been subtracted. The reduced χ^2 (χ^2_{red}) statistics for the spectral fits shown in (a) and (b) are 0.55 and 1.8, respectively.

In the work here, we perform a new normal mode analysis of L-Gln in order to assign our UVRR spectra. We employ DFT calculations that use a more modern functional (M06-2X) than that of Ramirez and co-workers. These assignments build off of our previous, detailed assignment of propanamide,[28] a model for the side chains of Gln and Asn. Our assignments of L-Gln in H_2O and D_2O are shown in Tables 1 and 2, respectively.

Table 1. UVRR Frequencies (cm^{-1}) and Assignments of L-Gln in H_2O

expt	calcd	potential energy distribution[a] (≥5% contribution)
1679	1745	$\nu C_\delta O_\epsilon$ (75), $-\nu C_\delta N_\epsilon$ (8), $\beta N_\epsilon C_\delta C_\gamma$ (7)
1652	1666	$\delta_{as}'NH_3$ (48), $-\delta_{as}NH_3$ (44), $-\rho NH_3$ (5)
1620	1623	$-\sigma N_\epsilon H_2$ (86), $-\nu C_\delta N_\epsilon$ (10)
	1621	$\delta_{as}NH_3$ (40), $\delta_{as}'NH_3$ (48), $\delta_s NH_3$ (10)
1585	1715	$-\nu CO$ (53), νCO (33), $\rho C_\alpha C$ (7)
1464	1494	$\sigma C_\beta H_2$ (88)
	1466	$-\delta_s NH_3$ (33), $\sigma C_\gamma H_2$ (30), $\omega C_\gamma H_2$ (7), $-\omega C_\beta H_2$ (5), $\nu C_\beta C_\gamma$ (5)
1447	1460	$-\sigma C_\gamma H_2$ (44), $-\delta_s NH_3$ (36)
1427	1445	$-\omega C_\gamma H_2$ (17), $\nu C_\alpha C_\delta$ (13), $\sigma C_\gamma H_2$ (13), $\omega C_\beta H_2$ (13), $-\nu C_\delta N_\epsilon$(9), $-\nu C_\beta C_\gamma$ (5), $-\delta_s NH_3$ (5), $\rho C_\delta O$ (5)
1411	1419	$-\nu CO$ (26), $\rho C_\alpha H$ (12), $\nu C_\alpha C$(11), $\omega C_\gamma H_2$ (8), βCOO (7), $\nu C_\delta N_\epsilon$ (7), $-\nu CO$ (7), $-\nu C_\gamma C_\delta$ (6)
1365	1388	$\rho C_\alpha H$ (25), $\omega C_\beta H_2$ (13), νCO (10), $-\rho' C_\alpha H$ (9), $\nu C_\alpha C_\beta$ (8), $-\tau C_\beta H_2$ (6), $-\nu C_\alpha C$ (5)
1351	1358	$-\rho C_\alpha H$ (30), $\omega C_\beta H_2$ (16), $-\tau C_\beta H_2$ (15), $\tau C_\gamma H_2$ (9), $\nu C_\delta N_\epsilon$ (6)
1328	1348	$-\tau C_\beta H_2$ (26), $-\omega C_\beta H_2$ (18), $-\rho' C_\alpha H$ (13), $-\nu C_\delta N_\epsilon$ (11)
1293	1309	$-\tau C_\gamma H_2$ (35), $-\rho' C_\alpha H$ (26), $\rho C_\beta H_2$ (8), $-\rho C_\alpha H$ (6)
1264	1272	$-\omega C_\gamma H_2$ (43), $-\omega C_\beta H_2$ (20), $\nu C_\delta N_\epsilon$ (13)
1206	1215	$-\tau C_\beta H_2$ (21), $-\nu C_\alpha C_\beta$ (18), $-\tau C_\gamma H_2$ (16), $-\rho' NH_3$ (13), $\delta NC_\alpha C(OO)$ (5)
1158	1153	$-\rho' C_\alpha H$ (20), $\tau C_\gamma H_2$ (17), $-\rho' NH_3$ (13), $\tau C_\beta H_2$ (12), $-\nu C_\alpha C_\beta$ (8), $\rho C_\gamma H_2$ (6)
1130	1122	$\nu C_\beta C_\gamma$ (34), $\rho N_\epsilon H_2$ (17), $-\nu C_\alpha C_\beta$ (7), $\nu C_\alpha N$ (6), $-\beta N_\epsilon C_\delta C_\gamma$ (5)
	1109	ρNH_3 (27), $-\rho' C_\alpha H$ (10), $-\rho N_\epsilon H_2$ (10), $-\delta' NCC(OO)$ (9), $-\rho C_\alpha H$ (7), $\nu C_\alpha N$ (7)
1110	1097	$\nu C_\beta C_\gamma$ (26), $-\rho N_\epsilon H_2$ (26), $-\nu C_\delta N_\epsilon$ (13), $-\rho NH_3$ (8)
	1038	$\nu C_\alpha N$ (36), $-\nu C_\beta C_\gamma$ (9), $\rho C_\beta H_2$ (8), $\rho' NH_3$ (6), $\rho C_\gamma H_2$ (5), $\rho' C_\alpha H$ (5)
1078	1003	ρNH_3 (25), $-\nu C_\alpha N$ (19), $\rho C_\gamma H_2$ (14), $\rho C_\beta H_2$ (14), $\nu C_\alpha C_\beta$ (7), $-\tau C_\beta H_2$ (5)
1006	974	$-\rho' NH_3$ (38), $\nu C_\alpha C_\beta$ (25), $-\nu C_\alpha C$ (8), $-\sigma CC_\alpha C_\beta$ (7), $\nu C_\alpha N$ (6)

[a] ν, stretch; δ_{as}, asymmetric deformation; δ_s, symmetric deformation; δ, deformation; σ, scissoring; ρ, rocking; ω, wagging; β, in-plane bending; τ, twisting.

The UVRR spectra are dominated by bands that derive from vibrations of the primary amide group. This is because these resonance enhanced vibrations couple to the strong ∼180 nm NV_1 electronic transition. These resonance enhanced amide bands contain significant contributions of C_δ–N_ϵ stretching because the electronic excited state is expanded along this coordinate.[53]

DOI: 10.1021/acs.jpcb.5b07651
J. Phys. Chem. B 2015, 119, 13039−13051

Table 2. UVRR Frequencies (cm^{-1}) and Assignments of L-Gln in D_2O

expt	calcd	potential energy distribution[a] (≥5% contribution)
1650	1739	$\nu C_\delta O_\epsilon$ (78), $-\nu C_\delta N_\epsilon$ (7), $\beta N_\epsilon C_\delta C_\gamma$ (7)
1637	1708	νCO (55), $-\nu$CO (34), $-\rho C_\alpha C$ (7)
1465	1494	$\sigma C_\beta H_2$ (88)
1453	1465	$-\sigma C_\gamma H_2$ (48), $-\omega C_\gamma H_2$ (15), $-\nu C_\beta C_\gamma$ (8), $-\nu C_\delta N_\epsilon$ (7), $\omega C_\beta H_2$ (6)
1440	1454	$-\sigma C_\gamma H_2$ (35), $\nu C_\delta N_\epsilon$ (19), $-\nu C_\gamma C_\delta$ (14), $\omega C_\gamma H_2$ (9), $-\rho C_\delta O_\epsilon$ (5)
1412	1424	$-\nu$CO (29), $\nu C_\alpha C$ (12), $-\nu$CO (10), $\omega C_\beta H_2$ (10), βCOO (9), $\nu C_\delta N_\epsilon$ (9), $\rho C_\alpha H$ (8)
1368	1393	$\omega C_\beta H_2$ (21), $\rho C_\alpha H$ (15), νCO (11), $\nu C_\alpha C_\beta$(8), $-\rho' C_\alpha H$ (6), νCO (6), $-\nu C_\alpha C$ (5), $\nu C_\delta N_\epsilon$ (5)
1344	1362	$-\rho C_\alpha H$ (37), $-\omega C_\gamma H_2$ (13), $\nu C_\delta N_\epsilon$ (12), $\omega C_\beta H_2$ (11), $\rho' C_\alpha H$ (7), $\sigma N_\epsilon D_2$ (5)
	1349	$-\tau C_\beta H_2$ (44), $\tau C_\gamma H_2$ (20), $-\rho C_\alpha H$ (15), $-\rho' C_\alpha H$ (6)
	1304	$-\rho' C_\alpha H$ (32), $-\tau C_\gamma H_2$ (29), $\rho C_\beta H_2$ (8), $-\rho C_\alpha H$ (7)
	1282	$-\omega C_\gamma H_2$ (37), $-\omega C_\beta H_2$ (33), $\sigma N_\epsilon D_2$ (8), $\rho C_\alpha H$ (7), $\nu C_\delta N_\epsilon$ (6)
	1202	$-\delta_{as}ND_3$ (23), $\delta_{as}'ND_3$ (20), $\tau C_\beta H_2$ (17), $\tau C_\gamma H_2$ (12), $\nu C_\alpha C_\beta$ (8)
	1198	$\delta_{as}ND_3$ (27), $\tau C_\beta H_2$ (12), $\tau C_\gamma H_2$ (11), $-\rho' C_\alpha H$ (9), $\nu C_\alpha C_\beta$(8), $\delta_s ND_3$ (7), $-\delta_{as}'ND_3$ (7)
	1186	$-\delta_{as}'ND_3$ (52), $-\delta_s ND_3$ (27), $-\nu C_\alpha N$ (8), $-\delta_{as}ND_3$ (6)
1161	1150	$\sigma N_\epsilon D_2$ (56), $\rho' C_\delta O_\epsilon$ (11), $\nu C_\gamma C_\delta$ (9), $\omega C_\gamma H_2$ (8)
	1131	$\nu C_\alpha C_\beta$(21), $-\delta_s ND_3$ (16), $-\nu C_\alpha N$ (14), $\delta_{as}ND_3$ (13), $-\tau C_\gamma H_2$ (5)
	1119	$-\nu C_\beta C_\gamma$ (17), $\delta_{as}ND_3$ (10), $\delta NC_\alpha C(OO)$ (9), $-\nu C_\alpha C_\beta$(8), $-\delta_s ND_3$ (8), $\sigma C_\gamma C_\beta C_\alpha$ (7), $-\nu C_\alpha N$ (6), $\delta_{as}'ND_3$ (5)
	1105	$\nu C_\beta C_\gamma$ (44), $-\delta_s ND_3$ (15), $\delta_{as}ND_3$ (8), $\delta_{as}'ND_3$ (6), $-\nu C_\alpha C_\beta$ (5)
	1058	$\rho C_\beta H_2$ (21), $\rho' C_\alpha H$ (16), $\rho C_\gamma H_2$ (12), $\delta' NC_\alpha C(OO)$ (9), $-\nu C_\alpha C$ (6), $\delta C' C_\alpha C_\beta$(6), $\nu C_\alpha C_\beta$(5), $-\rho ND_3$ (5)
992	998	$\nu C_\alpha N$ (29), $\delta_s ND_3$ (15), $-\delta' NC_\alpha C(OO)$ (10), $-\rho C_\alpha C$ (7), $-\nu C_\beta C_\gamma$ (5), $-\sigma CC_\alpha C_\beta$ (5)
960	959	$\rho N_\epsilon D_2$ (22), $\nu C_\delta N_\epsilon$ (14), $\nu C_\gamma C_\delta$ (10), $-\sigma N_\epsilon D_2$ (9), $-\nu C_\alpha N$ (9), $-\beta N_\epsilon C_\delta C_\gamma$ (8), $\nu C_\alpha C$ (6), $\nu C_\delta O_\epsilon$ (6)
929	920	$\nu C_\alpha C$ (17), $\rho C_\gamma H_2$ (16), ρND_3 (16), $-\tau C_\beta H_2$ (8), βCOO (8), $-\delta' NC_\alpha C(OO)$ (7), $\Pi N_\epsilon C_\delta C_\gamma$ (6)

[a] ν, stretch; δ_{as}, asymmetric deformation; δ_s, symmetric deformation; δ, deformation; σ, scissoring; ρ, rocking; ω, wagging; β, in-plane bending; τ, twisting; Π, out-of-plane deformation.

The spectral region between 1600 and 1700 cm^{-1} is dominated by two primary amide vibrations, the Amide I^P (AmI^P) and Amide II^P ($AmII^P$) bands. The superscript ^{P} denotes the primary amide to distinguish these vibrations from the widely known vibrations of secondary amides found in proteins. The AmI^P band is located at ~1680 cm^{-1} and derives mainly from $C_\delta{=}O_\epsilon$ stretching. In D_2O, the AmI^P band (called the AmI'^P) downshifts to ~1650 cm^{-1}. The $AmII^P$ band at ~1620 cm^{-1} derives from a vibration whose PED contains mostly $N_\epsilon H_2$ scissoring (~86%) and $C_\delta{-}N_\epsilon$ stretching (~10%). Upon N-deuteration, the $C_\delta{-}N_\epsilon$ stretching and ND_2 scissoring motions decouple. This causes the $AmII^P$ band to disappear, and a new band, which derives from $N_\epsilon D_2$ scissoring, appears at ~1160 cm^{-1}.

The most intense features of the Gln spectra in Figure 2 occur in the region between 1400 and 1500 cm^{-1}. Most of the bands found in this region derive from CH_2 scissoring or wagging modes. However, we assign the most intense band, located at ~1430 cm^{-1}, to a vibration that contains significant contributions of CH_2 wagging, $C_\gamma{-}C_\delta$ stretching, CH_2 scissoring, and $C_\delta{-}N_\epsilon$ stretching in its PED. This assignment is based on our previous work with propanamide,[28] which shows a similar intense band at ~1430 cm^{-1}.

The region between 1200 and 1400 cm^{-1} contains bands that derive mostly from $C_\alpha H$ rocking, CH_2 wagging, and CH_2 twisting modes. We assign the ~1365 and ~1350 cm^{-1} bands in the Figure 2a spectrum to $C_\alpha H$ rocking modes. We assign the strong bands located at ~1330 cm^{-1}, ~1290 cm^{-1}, and the very weak ~1205 cm^{-1} bands to CH_2 twisting modes. The ~1265 cm^{-1} feature is assigned to a CH_2 wagging vibration. Only two bands, at ~1370 and ~1345 cm^{-1}, appear in D_2O. We assign the ~1370 cm^{-1} band to a CH_2 wagging mode and the ~1345 cm^{-1} band to a $C_\alpha H$ rocking mode. We conclude that these vibrations appear strongly in the UVRR spectrum in Figure 2b because they contain significant $C_\delta{-}N_\epsilon$ stretching.

The region between 1000 and 1200 cm^{-1} contains bands that derive from vibrations with large C−C stretching, $N_\epsilon H_2$ rocking, or NH_3 rocking contributions. Most of the vibrations in this region are complex. We assign the ~1160 cm^{-1} band to a coupled $C_\alpha H$ rocking/CH_2 twisting mode. The PED of this vibration contains a significant contribution of NH_3 rocking, which likely accounts for the disappearance of this band upon N-deuteration. We assign the ~1080 and ~1005 cm^{-1} bands to NH_3 rocking vibrations.

The remaining two bands in the 1000−1200 cm^{-1} region are located at ~1130 and ~1110 cm^{-1}. The observed frequency difference between these two vibrations is ~20 cm^{-1}, which is close to the calculated ~25 cm^{-1} difference of our DFT calculations. We assign the 1130 cm^{-1} band to a vibration that is mainly an in-phase combination of $C_\beta{-}C_\gamma$ stretching and $N_\epsilon H_2$ rocking. The ~1110 cm^{-1} band is assigned to a vibration that consists of an out-of-phase combination of $C_\beta{-}C_\gamma$ stretching and $N_\epsilon H_2$ rocking. This vibration also contains a significant $C_\delta{-}N_\epsilon$ stretching component (~13%), which is in phase with $N_\epsilon H_2$ rocking.

The in-phase combination of $N_\epsilon H_2$ rocking and $C_\delta{-}N_\epsilon$ stretching of the ~1110 cm^{-1} vibration is reminiscent of the AmIII mode of secondary amides. While complex, the AmIII vibration contains significant contributions of in-phase C−N stretching and N−H in-plane bending motions of the secondary amide group. We propose to call the ~1110 cm^{-1} mode the Amide III^P ($AmIII^P$) because the eigenvector composition of this vibration is analogous to that of the canonical AmIII of secondary amides. As discussed in detail below, the $AmIII^P$ vibration is sensitive to the χ_3 and χ_2 dihedral angles of Gln and Asn.

Conformational Dependence of the $AmIII^P$ Band. We performed DFT calculations on L-Gln molecules with χ_3 dihedral angles fixed at different values (see Computational section for details) in order to identify spectroscopic markers that are diagnostic of the side chain χ_3 and χ_2 dihedral angles of Gln and Asn, respectively. We examined the frequency dependence of different primary amide vibrations and found that the $AmIII^P$ vibrational frequency and normal mode depends strongly on the OCCC dihedral angle.

Figure 3a shows the calculated cosinusoidal dependence of the $AmIII^P$ vibrational frequency on the χ_3 dihedral angle. The maximum frequency of the vibration occurs at $\chi_3 \sim 0°$, while minima occur near $\chi_3 \sim \pm 90°$. The Gln $AmIII^P$ band frequency dependence on the χ_3 angle follows a cosinusoidal relationship:

$$\nu(\chi_3) = \nu_0 + A\cos(2\chi_3) + B\cos(\chi_3 - C) \quad (1)$$

DOI: 10.1021/acs.jpcb.5b07651
J. Phys. Chem. B 2015, 119, 13039−13051

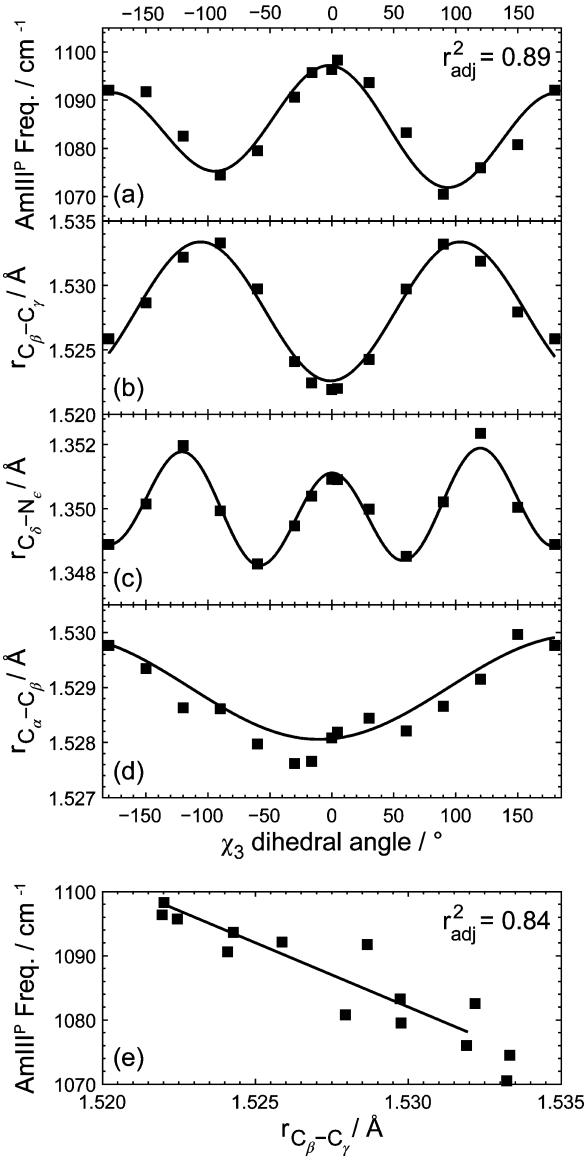

Figure 3. Calculated AmIII^P frequency and bond length dependence on the χ_3 dihedral angle of the Gln side chain. (a) AmIII^P frequency dependence, (b) C_β−C_γ bond length, (c) C_δ−N_ϵ bond length, (d) C_α−C_β bond length, and (e) the dependence of the AmIII^P frequency on the C_β−C_γ bond length.

where $\nu_0 = 1084\ \text{cm}^{-1}$, $A = 10\ \text{cm}^{-1}$, $B = 3\ \text{cm}^{-1}$, and $C = -31°$. These parameters were calculated from a least-squares fit of eq 1 to the frequency dependence on the χ_3 angle in Figure 3a.

Figure 3a shows that the AmIII^P frequency dependence on the χ_3 dihedral angle is asymmetric about $\chi_3 \sim 0°$. This asymmetry is due to the chirality of L-Gln and L-Asn and leads to the requirement of two cosine terms to express the χ_3 frequency dependence of eq 1. This is evident when we compare the L-Gln χ_3 dependence on the AmIII^P frequency with that of butyramide (shown in Supporting Information Figure S1). In the case of butyramide, which is achiral, there is no asymmetry about 0°. As a result, the AmIII^P frequency dependence on the OCCC dihedral angle of butyramide can be satisfactorily modeled with just one cosine term (Supporting Information eq S1).

Origin of the OCCC Dihedral Angle Dependence of the AmIII^P Vibration. Understanding the conformational dependence of the AmIII^P frequency on the primary amide OCCC dihedral angle requires a detailed knowledge of the atomic motions that give rise to the vibration. On the basis of our normal mode calculations of Gln, butyramide (Supporting Information Table S14), and propanamide,[28] we conclude that $N_\epsilon H_2$ rocking, C_δ−N_ϵ stretching, and C_β−C_γ stretching define the AmIII^P vibration. However, depending on the OCCC dihedral angle, other motions such as $C_\beta H_2$ twisting and C_α−C_β stretching can contribute to this vibration.

Therefore, we examined how the Gln C_δ−N_ϵ, C_β−C_γ, and C_α−C_β bond lengths change as a function of the χ_3 dihedral angle in order to understand the origin of the conformational sensitivity of the AmIII^P vibration. Changes in these bond lengths impact the AmIII^P frequency by affecting the vibrational mode bond force constants. As seen in Figure 3b−d, all the bond lengths show a dependence on the χ_3 dihedral angle. However, as seen in Figure 3b, the C_β−C_γ bond length shows the largest dependence on the χ_3 dihedral angle. The AmIII^P vibrational frequency has a strong correlation with the C_β−C_γ bond length, as shown in Figure 3e. The AmIII^P vibrational frequency increases as the C_β−C_γ bond length decreases and vice versa.

The C_β−C_γ bond length dependence on the χ_3 dihedral angle appears to be due to hyperconjugation between the C_β−C_γ σ and the C_δ═O_ϵ π^* orbitals (Figure 4). This interaction is strongest when these orbitals maximally overlap in the absence of significant phase cancellation due to the π^* orbital antisymmetry. When hyperconjugation occurs, the σ orbital donates electron density to the π^* orbital, which decreases the C_β−C_γ bond order and increases its bond length. This decreases the C_β−C_γ stretching force constant, which downshifts the AmIII^P frequency.

We tested this hypothesis with natural bond orbital (NBO) analysis, which allows the DFT calculated electron densities to be displayed in terms of approximate σ and π^* molecular orbitals. According to our hypothesis, the C_β−C_γ bond length should be largest when hyperconjugation is maximized and smallest when there is no hyperconjugation. Indeed, as seen in Figure 4b, there is significant overlap of the C_β−C_γ σ and C_δ═O_ϵ π^* NBO molecular orbitals at ±90°, where the C_β−C_γ bond length is largest. In contrast, at $\chi_3 \sim 0°$, where the C_β−C_γ bond length is shortest, the orbital overlap cancels due to the antisymmetry of the π^* orbital. Figure 5 shows the NBO charge on the C_β atom. As expected from our hyperconjugation hypothesis, the NBO C_β atom charge is less negative at $\chi_3 \sim \pm 90°$ compared to $\chi_3 \sim 0°$. The NBO C_β atom charge becomes even more negative at $\chi_3 \sim \pm 150°$ and $\chi_3 \sim \pm 180°$, even without additional hyperconjugation of the C_β−C_γ σ and C_δ═O_ϵ π^* orbitals. This result is likely an artifact because these extreme χ_3 dihedral angles are associated with physically impossible high energy structures that will be subject to other electron density alterations.

Our model accounts for the AmIII^P frequency downshift as the dihedral angles approach $\chi_3 \sim \pm 90°$, where hyperconjugation is strongest. This behavior is the reverse of the Bohlmann effect,[54−57] where a "negative" hyperconjugation transfers electron density from a lone pair orbital to an optimally positioned C−H σ^* orbital. This decreases the C−H bond order and substantially downshifts the C−H stretching frequencies.

Experimental Dependence of AmIII^P Band Frequency on OCCC Dihedral Angle. We experimentally examined the dependence of the AmIII^P band frequency on the primary

DOI: 10.1021/acs.jpcb.5b07651
J. Phys. Chem. B 2015, 119, 13039−13051

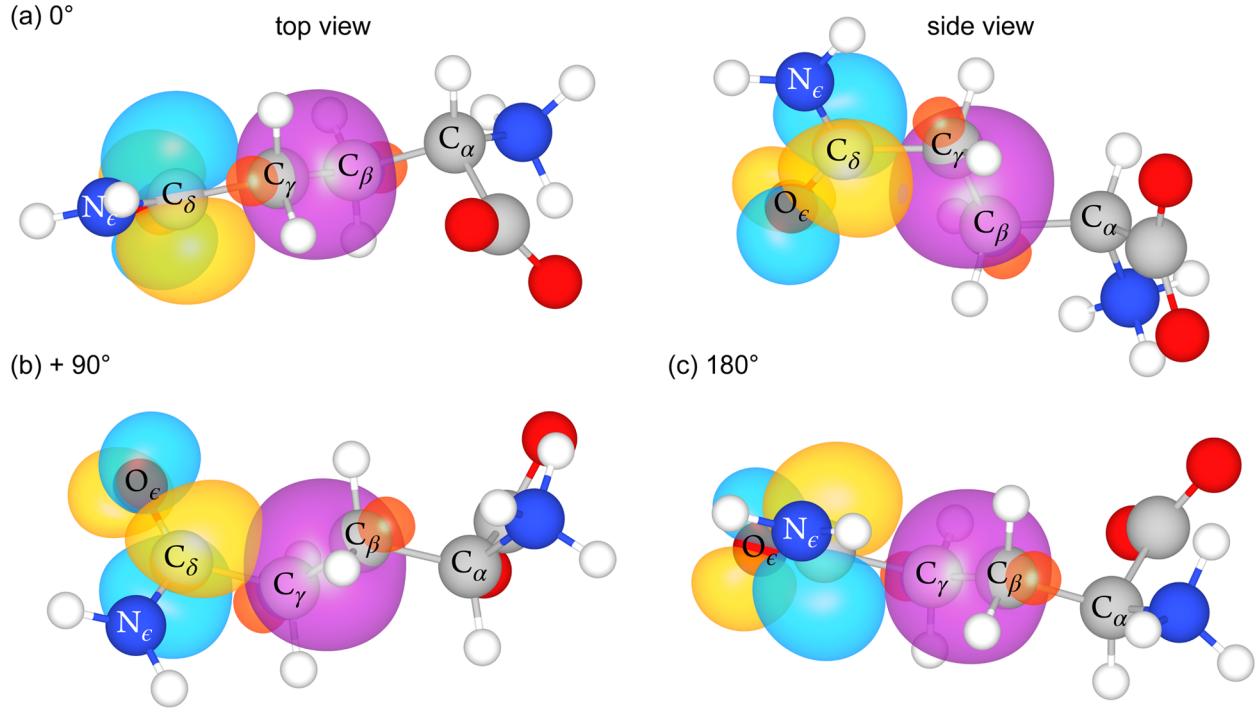

Figure 4. Hyperconjugation results in the C_β–C_γ bond length sensitivity to the χ_3 dihedral angle. Overlap of C_β–C_γ σ and C_δ=O_ϵ π^* NBO molecular orbitals when the χ_3 dihedral angle is (a) 0°, (b) +90°, and (c) ±180°.

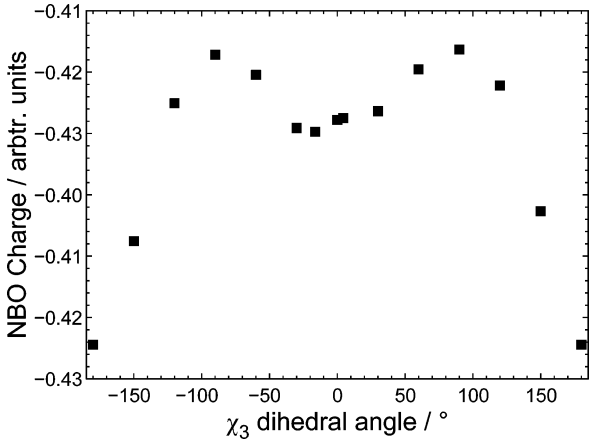

Figure 5. NBO charge of C_β in L-Gln as a function of the χ_3 dihedral angle.

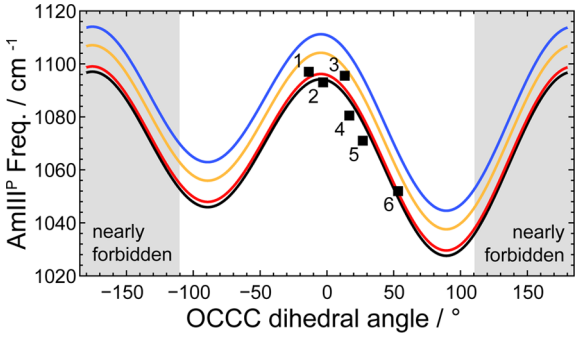

Figure 6. Experimental correlation of the AmIII^P frequency to the χ_3 dihedral angle. The average frequency (from the 633 and 229 nm Raman spectra) of the AmIII^P band was plotted as a function of the OCCC dihedral angle: 1 = L-Gln, 2 = Gly-Gln, 3 = D-Gln, 4 = GlnTBE, 5 = NAcGln, and 6 = Ser-Asn. The data were fit with eq 2 (black line, r^2_{adj} = 0.83). The blue curve corresponds to eq 3. The red curve corresponds to eq 4. The yellow curve corresponds to eq 5 and is an average of the red and blue curves.

amide OCCC dihedral angle by measuring the UVRR and visible Raman spectra of different Gln and Asn derivatives in the solid-state. We determined the structures of each of the different Gln and Asn derivative crystals with X-ray diffraction and assigned the AmIII^P band by performing DFT calculations and examining band shifts upon N-deuteration. Our X-ray diffraction methods and the band assignments of the crystals are discussed, in detail, in the Supporting Information.

Dependence of AmIII^P Band Frequency in Crystals. Figure 6 shows the AmIII^P frequency dependence on the experimentally determined primary amide OCCC dihedral angles. We fit the experimental data to a function of the same form as eq 1, obtaining the following relationship:

$$\nu(\chi_3) = 1066(\mathrm{cm}^{-1}) + 29(\mathrm{cm}^{-1})\cos(2\chi_3) + 9(\mathrm{cm}^{-1})\cos(\chi_3 + 99°) \quad (2)$$

which is shown in the Figure 6 black curve. To obtain the eq 2 parameters, we fixed the A/B ratio to ∼3 as found in eq 1 and performed a least-squares minimization of the experimental data. Equation 2 provides an excellent fit of the experimental data and captures the chiral asymmetry that occurs near χ_3∼ ±90°.

Dependence of AmIII^P Band Frequency for Fully Hydrated Primary Amides. The AmIII^P band frequency also depends on the local hydrogen bonding and dielectric environment of the primary amide group.[28] In water, the AmIII^P band of L-Gln is located at ∼1110 cm^{-1}, as compared with ∼1097 cm^{-1} in the solid-state. On the basis of Rhys et al.'s neutron diffraction study,[58] the solution-state equilibrium structure of L-Gln in water does not appear to differ significantly from the single known L-Gln crystal structure.[59] From their solution-state

DOI: 10.1021/acs.jpcb.5b07651
J. Phys. Chem. B 2015, 119, 13039−13051

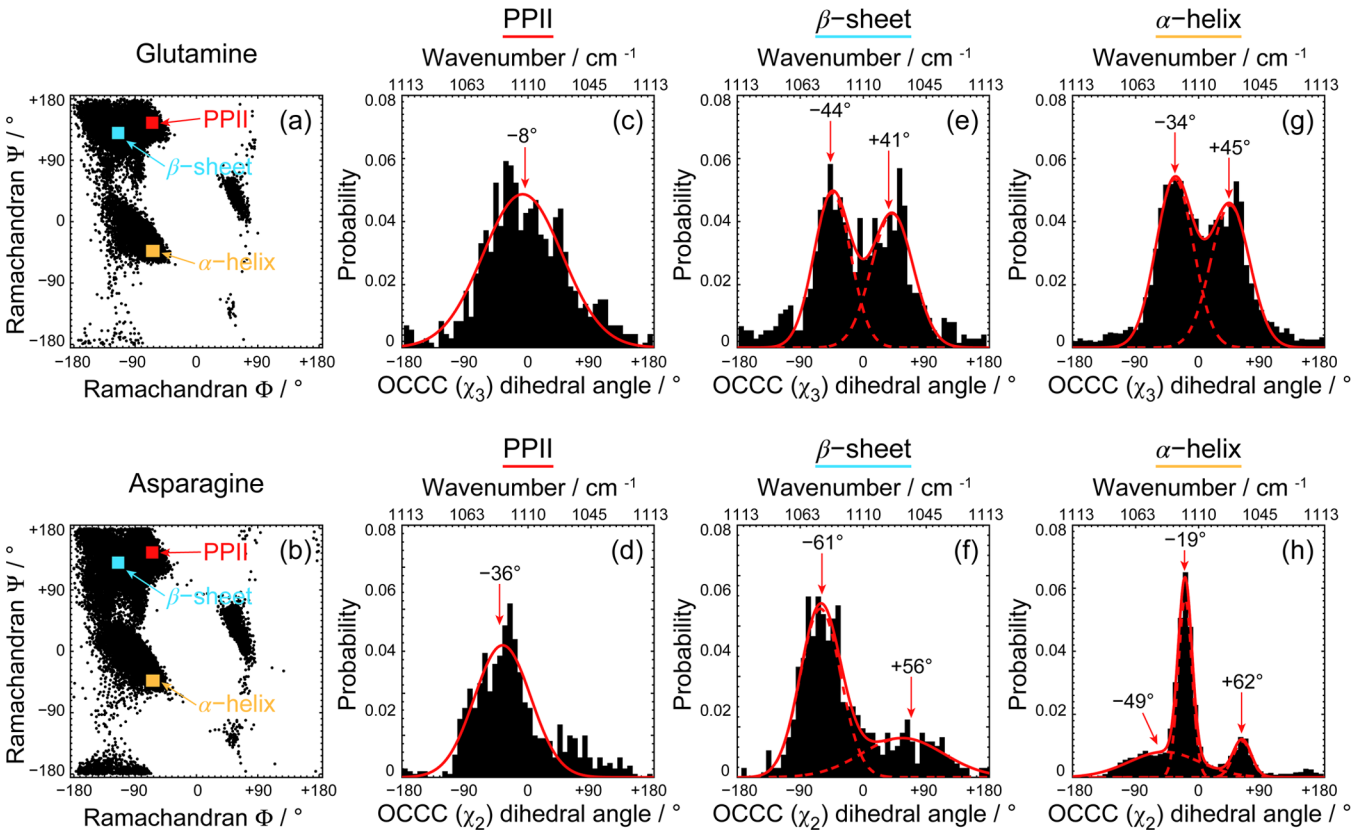

Figure 7. Gln and Asn side chain χ_3 and χ_2 dihedral angle dependence on secondary structure. Plots showing Ramachandran angles for PDB entries from the Shapovalov and Dunbrack database of (a) Gln and (b) Asn. The colored boxes correspond to canonical PPII ($\Phi = -65°$, $\Psi = 145°$) angles (red), β-sheet ($\Phi = -115°$, $\Psi = 130°$) angles (blue), and α-helix ($\Phi = -63°$, $\Psi = -43°$) angles (yellow). Distributions of χ_3 and χ_2 dihedral angles for Gln and Asn residues that have (Φ, Ψ) angles close to canonical: (c,d) PPII-like, (e,f) β-sheet, and (g,h) α-helical structures.

structure, we determine that the equilibrium χ_3 dihedral angle of L-Gln in water is $\sim -12.8°$. This differs by less than a degree ($-13.54°$) from the L-Gln crystal examined in this study. Thus, by setting the AmIII^P frequency to 1110 cm^{-1}, χ_3 to $-13.54°$, and solving for ν_0, we obtain eq 3:

$$\nu(\chi_3) = 1083(\text{cm}^{-1}) + 29(\text{cm}^{-1})\cos(2\chi_3) + 9(\text{cm}^{-1})\cos(\chi_3 + 99°) \quad (3)$$

which is shown by the Figure 6 blue curve. This equation correlates the AmIII^P band frequency to OCCC dihedral angles for situations in which the primary amide group is fully exposed to water, such as in polyproline II-like (PPII-like) structures, 2.5$_1$-helices,[60] and extended β-strand-like peptide conformations dissolved in water.

Dependence of AmIII^P Band Frequency for Low Dielectric Constant and Weak Hydrogen Bonding Environments. The AmIII^P frequency downshifts $\sim$15 cm^{-1} in the low dielectric and hydrogen bonding environment of acetonitrile compared to that in water (see Supporting Information and Figure S6). This downshift derives from the different water versus acetonitrile stabilizations of the ground state $O_\epsilon{=}C_\delta N_\epsilon H_2$ and $^-O_\epsilon C_\delta{=}N_\epsilon H_2^+$ resonance structures of the primary amide group.[28] In both solvents, the $O_\epsilon{=}C_\delta N_\epsilon H_2$ resonance structure dominates; however, in acetonitrile, the $^-O_\epsilon C_\delta{=}N_\epsilon H_2^+$ resonance structure contributes less than in water. Thus, the $C_\delta{-}N_\epsilon$ bond length is larger in acetonitrile compared to water due to the lesser favorability of the $^-O_\epsilon C_\delta{=}N_\epsilon H_2^+$ resonance structure. Consequently, there is a smaller $C_\delta{-}N_\epsilon$ stretching force constant in acetonitrile compared to water, which results in a downshift of the AmIII^P frequency.

Equation 3 can be modified in order to account for situations where the primary amide group is not engaged in significant hydrogen bonding interactions or when located in a low dielectric environment. We apply a 15 cm^{-1} downshift in ν_0 from eq 3 to determine eq 4:

$$\nu(\chi_3) = 1068(\text{cm}^{-1}) + 29(\text{cm}^{-1})\cos(2\chi_3) + 9(\text{cm}^{-1})\cos(\chi_3 + 99°) \quad (4)$$

which is shown in red in Figure 6.

Dependence of AmIII^P Band Frequency for Unknown Dielectric and Hydrogen Bonding Environments. We suggest the use of eq 5, which is the average of eqs 3 and 4, for cases where the hydrogen bonding and dielectric environment of the primary amide group is unknown:

$$\nu(\chi_3) = 1076(\text{cm}^{-1}) + 29(\text{cm}^{-1})\cos(2\chi_3) + 9(\text{cm}^{-1})\cos(\chi_3 + 99°) \quad (5)$$

It can be applied, for example, to determine the side chain χ_3 and χ_2 dihedral angles of Gln and Asn residues located in turn structures of proteins. For these residues, it may not be clear if the side chains are hydrogen bonded to water, to other side chains, or the peptide backbone. Equation 5 is shown by the yellow curve in Figure 6.

Predicting Side Chain χ_3 and χ_2 Dihedral Angles in Gln and Asn as a Function of Ramachandran (Φ, Ψ) Angles.

DOI: 10.1021/acs.jpcb.5b07651
J. Phys. Chem. B 2015, 119, 13039−13051

Table 3. Predicted AmIII^P Frequencies and OCCC Dihedral Angles for Gln and Asn Residues with Different Ramachandran Angles

			Gln		Asn	
	Φ (deg)	Ψ (deg)	χ_3 (deg)	AmIII^P freq (cm^{-1})	χ_2 (deg)	AmIII^P freq (cm^{-1})
PPII	−65	145	−8 (−22, −32)[a]	1111 (1106, 1099)[a]	−36	1096
β-sheet	115	130	−44, 41	1089, 1080	−6, 56	1075, 1064
α-helix	−63	−43	−34, 45	1098, 1076	−49, −19, 62	1085, 1107, 1058

[a]Values in parentheses were measured experimentally for Gln_3 and Asp_2-Gln_{10}-Lys_2.

Shapovalov and Dunbrack[44] recently developed a new peptide backbone dependent rotamer library, which includes the nonrotameric Gln and Asn side chain χ_3 and χ_2 dihedral angles. Their database was compiled by analyzing high resolution crystal structures from the Protein Data Bank (PDB) and consists of ∼30000 entries for Asn and ∼20000 entries for Gln. Parts a and b of Figure 7 show Ramachandran plots of all of the Gln and Asn entries in the Shapovalov and Dunbrack database. The Gln and Asn side chains populate similar regions of the Ramachandran plot, and both show a preference for α-helical region (Φ, Ψ) angles. Asn populates a much broader range of (Φ, Ψ) angles, especially in the nearly forbidden "bridge" region between β-sheet and α-helical regions of the Ramachandran plot.

We used the Shapovalov and Dunbrack database to examine the side chain χ_3 and χ_2 dihedral angle preferences of Gln and Asn residues that possess canonical PPII, β-sheet, or α-helix Ramachandran angle values. On the basis of work by Richardson[61] and Karplus,[62] we assume (Φ, Ψ) angles centered around (−65°, 145°) for canonical PPII structures, (−115°, 130°) for canonical β-sheets and (−63°, −43°) for canonical α-helices. Parts c−h of Figure 7 depict histograms of the χ_3 and χ_2 dihedral angles observed for the population of Gln and Asn residues with canonical PPII, β-sheet or α-helical Ramachandran angles.

The Gln and Asn side chain χ_3 and χ_2 dihedral angles clearly depend upon the peptide bond Φ and Ψ angles. This correlation could result from a preference for particular χ_3 or χ_2 dihedral angles for stretches of consecutive peptide bonds with (Φ, Ψ) angles that result in PPII, β-sheet, or α-helical secondary structures. Alternatively, it could result from a preference for χ_3 or χ_2 dihedral angles for the (Φ, Ψ) angle values of their individual peptide bonds.

The χ_3 and χ_2 dihedral angle histograms of Gln and Asn residues that populate the canonical PPII region of the Ramachandran plot are shown in Figure 7c,d. The distribution of χ_3 angles adopted by Gln is broader than that of the χ_2 angles of Asn. Both histograms are centered about negative dihedral angles, with Gln showing a peak at around $\chi_3 \sim -8°$ and Asn showing a peak near $\chi_2 \sim -36°$. It should be noted that the bias due to the L-amino acid chirality gives rise to a clear preference for negative χ_2 dihedral angles for the shorter side chain Asn residues.

The χ_3 and χ_2 dihedral angle histograms of Gln and Asn with β-sheet (Φ, Ψ) angles in Figure 7e,f differ dramatically from one another. The population of Gln χ_3 dihedral angles (Figure 7e) is nearly symmetric about $\chi_3 \sim 0°$. The histogram is bimodal, with two peaks located near χ_3 angles of ∼ −44° and ∼41°. In contrast, the population of Asn residues (Figure 7f) predominately adopts negative dihedral angles and is peaked around $\chi_2 \sim -61°$. A minor peak also occurs around $\chi_2 \sim 56°$.

Parts g and h of Figure 7 show histograms of the χ_3 and χ_2 dihedral angles of Gln and Asn residues that adopt canonical α-helical Ramachandran angles. As in Figure 7e, the Figure 7g Gln χ_3 dihedral angle population is roughly bimodal and nearly symmetric about $\chi_3 \sim 0°$. It is peaked at χ_3 angles of ∼ −34° and ∼45°. In contrast, in Figure 7h, the population of Asn χ_2 dihedral angles is narrow and sharply peaked at $\chi_2 \sim -19°$ with two minor peaks at $\chi_2 \sim -49°$ and ∼62°.

The χ_3 and χ_2 dihedral angle dependencies on the peptide bond Ramachandran angles, shown by the Shapovalov and Dunbrack database, enable us to predict the most probable AmIII^P frequencies of Gln and Asn residues that adopt canonical PPII, β-sheet, and α-helix (Φ, Ψ) angles (shown in Table 3). For example, using eq 3, we calculate that Gln and Asn side chains with PPII (Φ, Ψ) angles will have a maximum probability of showing AmIII^P bands centered at ∼1111 cm^{-1} and ∼1096 cm^{-1}, respectively. Similarly, we calculate that the AmIII^P bands of Gln residues with β-sheet Ramachandran angles will have the greatest probability of being located at ∼1080 cm^{-1} and/or ∼1089 cm^{-1}. In contrast, the AmIII^P bands for Asn residues with β-sheet (Φ, Ψ) angles will have the largest probability of being located at ∼1064 cm^{-1} and/or ∼1075 cm^{-1}. For α-helical Ramachandran angles, we calculate that the probability maxima for AmIII^P bands will be at ∼1076 cm^{-1} and/or ∼1098 cm^{-1} for Gln and ∼1058, ∼1085, and/or ∼1107 cm^{-1} for Asn residues.

We can calculate the expected Raman spectral AmIII^P band shapes from the Gln χ_3 and Asn χ_2 dihedral angle histograms in Figure 7 using the AmIII^P Raman band frequency dependencies of eqs 2−5. These calculated band shapes (not shown) are unphysically broad (>100 cm^{-1}). This clearly indicates that these histograms derive from the inhomogeneous distribution of χ_3 and χ_2 angles of individual Gln and Asn residues within the proteins found in the Shapovalov and Dunbrack database. This distribution of Raman frequencies from the calculated AmIII^P band is much broader than the homogeneous line width of an AmIII^P band expected for a single Gln and Asn residue in a typical PPII, β-sheet, or α-helix conformation in proteins. The large widths of the Gln χ_3 and Asn χ_2 dihedral angle histograms result because the residues in the Shapovalov and Dunbrack database exist in a larger distribution of conformations, hydrogen bonding states, and chemical environments than we have so far encountered in our UVRR investigations.

Experimentally Determined Gln PPII-like Structure Peptide χ_3 Dihedral Angles. *UVRR Spectra of Gln Peptides in PPII-like Structures.* We examined the UVRR spectra of two peptides, Gln_3 and Asp_2-Gln_{10}-Lys_2, in order to determine their solution-state χ_3 angles. Xiong et al.[30] previously showed that Asp_2-Gln_{10}-Lys_2 exists in predominately PPII-like and 2.5_1-helix-like conformations when prepared using a "disaggregation" protocol developed by Wetzel and co-workers.[63] In this protocol, the Asp_2-Gln_{10}-Lys_2 peptide is initially dissolved in a mixture of trifluoroacetic acid and hexafluoroisopropanol. These solvents are subsequently evaporated under dry N_2 gas, and the peptide is redissolved in pure water.

DOI: 10.1021/acs.jpcb.5b07651
J. Phys. Chem. B 2015, 119, 13039−13051

The UVRR spectra indicate that Gln_3 has predominately PPII-like peptide bond conformations. Figure 8a shows the peak fitted ~204 nm excitation UVRR spectrum of Gln_3 in the region between 1050 and 1500 cm^{-1}. The $AmIII_3$ region, between ~1200 and 1280 cm^{-1}, is most sensitive to the secondary structure of the peptide because its frequency depends on the Ramachandran Ψ angle.[35,37] This region is well fit by two Gaussian bands located at ~1210 and ~1260 cm^{-1}. Using the methodology of Mikhonin et al.,[37] we correlated the band peak positions to their Ψ angles. We used their eq 6A to correlate the 1210 cm^{-1} frequency of the $AmIII_3$ band to a Ψ angle of 103° ± 3° and the 1260 cm^{-1} frequency to a Ψ angle of 157° ± 2°. The Ψ angle of ~157° derives from peptide bonds situated in PPII-like conformations, while the Ψ angle of ~103° derives from peptide bond situated in β-strand-like conformations. Assuming identical Raman cross sections for these two different species, we find that the peptide bonds are dominated by PPII-like Ψ angles (~87 ± 2%), while a small fraction adopt β-strand-like Ψ angles (~13 ± 2%). This is supported by the circular dichroism spectra of Gln_3 shown in Supporting Information Figure S7, which show a predominantly PPII spectral signature.

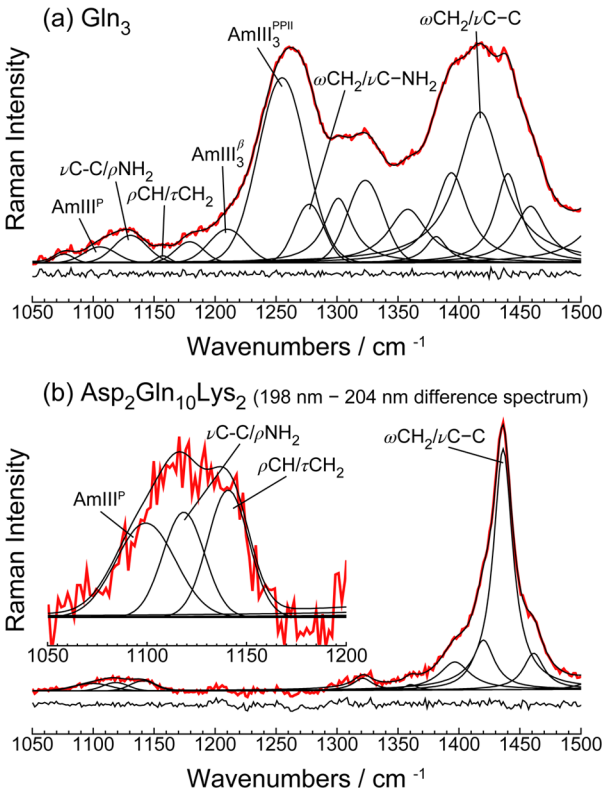

Figure 8. Deconvolution of the UVRR spectra of Gln_3 and Asp_2-Gln_{10}-Lys_2. (a) Fitting the 204 nm excitation UVRR spectrum of Gln_3. (b) The 198−204 nm difference spectrum of Asp_2-Gln_{10}-Lys_2 taken from Xiong et al.[30] The inset shows the $AmIII^P$ region of Asp_2-Gln_{10}-Lys_2. The χ^2_{red} statistics for the spectral fits shown in (a) and (b) are 1.1 and 0.74, respectively.

χ_3 Dihedral Angle Determination of Side Chains in Gln Peptides. The $AmIII^P$ bands of Gln_3 and Asp_2-Gln_{10}-Lys_2 are found in the region between ~1050 and 1150 cm^{-1}. On the basis of our normal mode analysis of Gln, we fit this region for Gln_3 with four bands that derive from $C_\alpha H$ rocking/$C_\gamma H_2$ twisting, C_β−C_γ stretching/$N_\epsilon H_2$ rocking, NH_3 rocking/C_α−N stretching, and the $AmIII^P$ vibrations. For Gln_3, these bands are located within a broad asymmetric spectral feature at ~1080, ~1106, ~1130, and ~1160 cm^{-1}.

We assign these Gln_3 bands based on our analysis of Gln. We assign the ~1160 cm^{-1} band to a $C_\alpha H$ rocking/$C_\gamma H_2$ twisting mode, the ~1130 cm^{-1} band to a C_β−C_γ stretching/$N_\epsilon H_2$ rocking vibration, and the ~1080 cm^{-1} band to a NH_3 rocking/C_α−N stretching mode. The ~1106 cm^{-1} band appears as a low-frequency shoulder feature and is assigned to the $AmIII^P$ vibration. This is very close to the predicted $AmIII^P$ vibrational frequency band center from the Gaussian fit of PPII-like structures in Figure 7c, as listed in Table 3. In fact, the $AmIII^P$ frequency band center of Gln_3 differs by only ~5 cm^{-1} from the predicted frequency band center (~1111 cm^{-1}) for PPII Ramachandran angles.

Figure 8b shows the 198−204 nm difference spectrum of disaggregated Asp_2-Gln_{10}-Lys_2 published by Xiong et al.[30] Xiong et al. showed that excitation at 198 nm enhances the primary amide UVRR bands more than does excitation at 204 nm. Thus, the Figure 8b Asp_2-Gln_{10}-Lys_2 difference spectrum is dominated by the primary amide Gln side chain bands with little interference from the secondary amide peptide bond UVRR bands.

The inset in Figure 8b shows the region where the $AmIII^P$ band of Asp_2-Gln_{10}-Lys_2 is located. We parsimoniously peak fit this region to three Gaussian bands located at ~1099, ~1118, and ~1140 cm^{-1}. Using prior knowledge from our analysis of Gln, we assign the bands at ~1118 and ~1140 cm^{-1} to the C_β−C_γ stretching/$N_\epsilon H_2$ rocking and $C_\alpha H$ rocking/$C_\gamma H_2$ twisting vibrations, respectively. The ~1099 cm^{-1} band is assigned to the $AmIII^P$ band.

The $AmIII^P$ bandwidths of Gln_3 and Asp_2-Gln_{10}-Lys_2 are ~30 cm^{-1}, which is similar to that of Gln in H_2O (Figure 2a). These bandwidths are roughly twice as large as those found in the Raman spectra of the different Gln and Asn derivative crystals, which we measure to be on average ~13.3 ± 5.0 cm^{-1}. This bandwidth is significantly larger than our spectrometer resolution of ~4.5 cm^{-1}. Thus, if we assume a Lorentzian band shape, we estimate that the $AmIII^P$ band homogeneous line width for a Gln compound with a well-defined χ_3 angle is ~6.6 cm^{-1}. The fact that the $AmIII^P$ bandwidths of solution-state Gln, Gln_3, and Asp_2-Gln_{10}-Lys_2 are much broader than those measured in our crystals suggests that there is a distribution of hydrogen bonding states and χ_3 angles in these compounds.

Given the estimated homogeneous line width, we can roughly calculate the distribution of χ_3 angles of Gln, Gln_3, and Asp_2-Gln_{10}-Lys_2 by using a methodology that is similar to that of Asher et al.[36] To do this, we assume that the inhomogeneously broadened $AmIII^P$ bands derive from a distribution of different χ_3 dihedral angles, which can be represented as the sum of M Lorentzian bands:

$$A(\nu) = \frac{1}{\pi}\sum_{i=1}^{M} I_i \frac{\Gamma^2}{\Gamma^2 + (\nu - \nu_i)^2} \tag{6}$$

where I_i is the intensity of a Lorentzian band that occurs at a given center frequency, ν_i, and Γ is the homogeneous line width.

We can apply eq 3 to correlate the ν_i $AmIII^P$ frequencies of the M Lorentzian bands to their corresponding χ_3 dihedral angles. As shown in Figure 6, a single $AmIII^P$ frequency can correspond to as many as four possible χ_3 dihedral angles.

DOI: 10.1021/acs.jpcb.5b07651
J. Phys. Chem. B 2015, 119, 13039−13051

However, the Shapovalov and Dunbrack database show that χ_3 dihedral angles that are greater than +90° and less than −90° are nearly forbidden (Figure 7). Thus, we consider only the two χ_3 dihedral angle solutions that are found in the region between −90° and +90°, as shown in Figure 9.

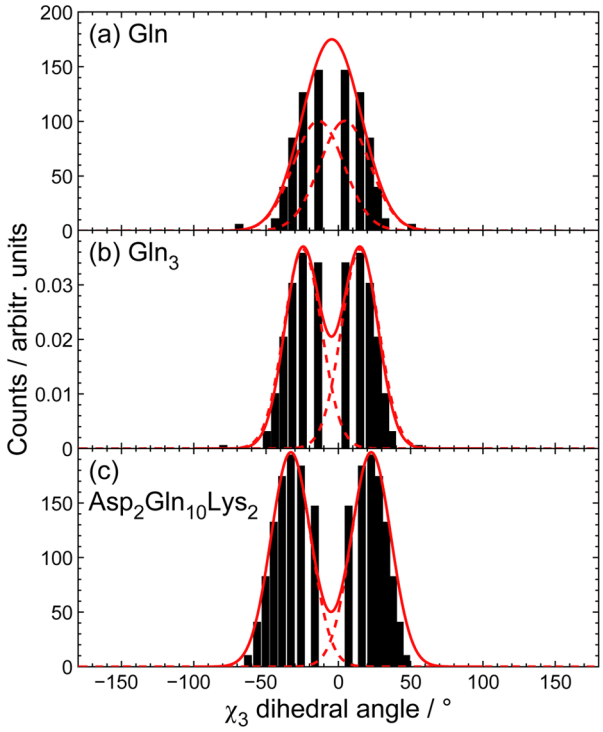

Figure 9. χ_3 dihedral angle historgrams calculated by decomposing AmIII^P bands into a sum of Lorentzians for (a) Gln, (b) Gln_3, and (c) Asp_2-Gln_{10}-Lys_2 in water. Because the solution to eq 3 is double valued between ±90°, the histograms show two peaks. The histograms were fit to two identical Gaussians that differed only in center χ_3 dihedral angles (shown in dashed lines). The sum of the Gaussians is shown in the solid red lines.

To determine which of the two remaining χ_3 dihedral angle solutions is occurring in our peptides, we first fit the histograms to the sum of two Gaussians with identical amplitudes, A, and widths, w, but different center χ_3 angles, $\overline{\chi}_{3,1}$ and $\overline{\chi}_{3,2}$:

$$I(\chi_3) = Ae^{-\left(\frac{\chi_3-\overline{\chi}_{3,1}}{w}\right)^2} + Ae^{-\left(\frac{\chi_3-\overline{\chi}_{3,2}}{w}\right)^2} \tag{7}$$

The Gln, Gln_3, and Asp_2-Gln_{10}-Lys_2 results all show one Gaussian centered at negative χ_3 angles and another Gaussian centered at positive χ_3 angles (Figure 9). For Gln, we assume that the Gaussian centered at $\chi_3 \sim -13°$ is the physically relevant solution based on the neutron diffraction study of Rhys et al.[58] For Gln_3 and Asp_2-Gln_{10}-Lys_2, we conclude that the Gaussians centered at negative χ_3 angles correspond to the physically relevant solutions to eq 3 because they fall within the range of χ_3 dihedral angles most commonly adopted by Gln residues that populate PPII (Φ, Ψ) angles (Figure 7c).

Figure 10 shows the resulting χ_3 dihedral angle distributions for Gln, Gln_3, and Asp_2-Gln_{10}-Lys_2 by assuming the physically relevant solutions to eq 3. The distributions of Gln_3 and Asp_2-Gln_{10}-Lys_2 populate χ_3 angles similar to that of Gln. This suggests that primary amides of Gln_3 and Asp_2-Gln_{10}-Lys_2 are fully solvated like that of monomeric Gln in water. Thus, the

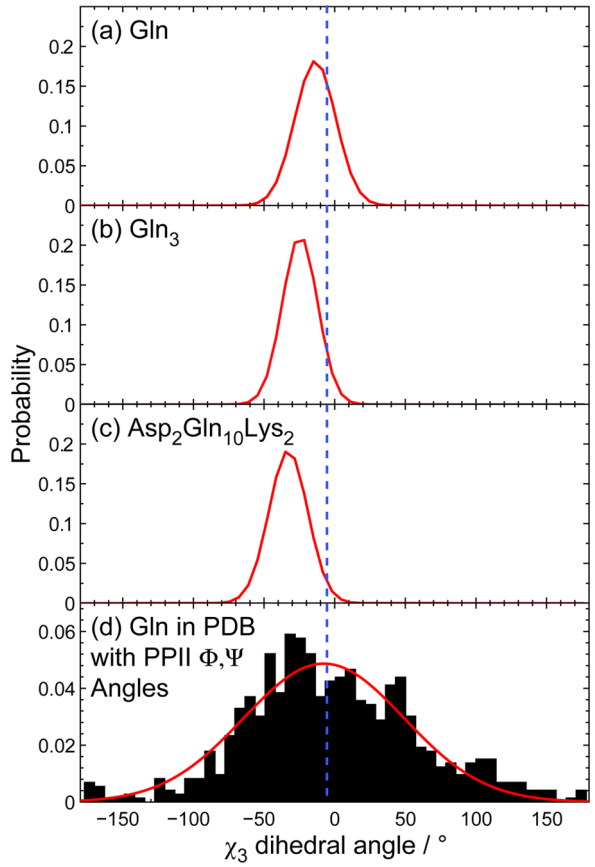

Figure 10. Comparison of χ_3 dihedral angle distributions between (a) Gln, (b) Gln_3 in a predominately PPII-like conformation, and (c) Asp_2-Gln_{10}-Lys_2 in a PPII/2.5_1-helix equilibrium. (d) χ_3 angle distribution of Gln residues with PPII-like Ramachandran angles from the Shapovalov and Dunbrack database.

Gln side chains are not engaged in side chain−backbone peptide bond hydrogen bonding as previously hypothesized.[64]

Determination of the Gibbs Free Energy Landscape for Gln and Gln Peptides along the χ_3 Dihedral Angle Reaction Coordinate. The structure sensitivity of the AmIII^P band enables us to determine the Gibbs free energy landscape of the Gln side chains along the χ_3 dihedral angle structure coordinate. To do this, we assume that the probability of each $\chi_{3,i}$ angle in the χ_3 dihedral angle distributions of Gln, Gln_3, and Asp_2-Gln_{10}-Lys_2 shown in Figure 10a−c is given by a Boltzmann distribution:

$$\frac{p(\chi_{3,i})}{p(\chi_{3,0})} = e^{-(\Delta G(\chi_{3,i})/RT)} \tag{8}$$

where $p(\chi_{3,i})/p(\chi_{3,0})$ is the ratio of populations with χ_3 angles $\chi_{3,i}$ and $\chi_{3,0}$. The angle, $\chi_{3,0}$, is the minimum energy χ_3 angle, R is the molar gas constant, T is the experimental temperature (293 K), and $\Delta G(\chi_{3,i}) = G(\chi_{3,i}) - G(\chi_{3,0})$. We assume in eq 8 that each $\chi_{3,i}$ dihedral angle state has a degeneracy of one.

To calculate the free energy difference, $\Delta G(\chi_{3,i})$, between a particular $\chi_{3,i}$ angle and the equilibrium $\chi_{3,0}$ angle, we rearrange eq 8:

$$\Delta G(\chi_{3,i}) = -RT \ln\left[\frac{p(\chi_{3,i})}{p(\chi_{3,0})}\right] \tag{9}$$

DOI: 10.1021/acs.jpcb.5b07651
J. Phys. Chem. B 2015, 119, 13039−13051

Figure 11 shows the calculated Gibbs free energy landscapes of Gln, Gln_3, and Asp_2-Gln_{10}-Lys_2 along the χ_3 dihedral angle

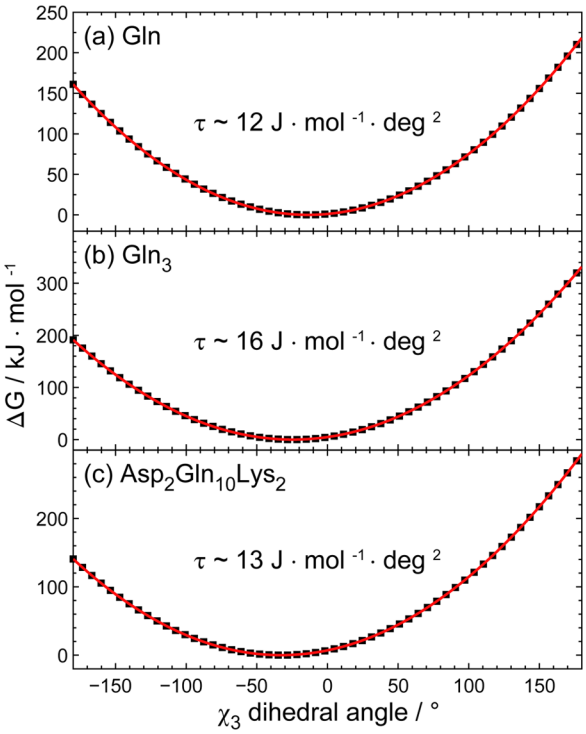

Figure 11. Gibbs free energy landscapes of (a) Gln, (b) Gln_3, and (c) Asp_2-Gln_{10}-Lys_2. The energy wells can be modeled by assuming a harmonic oscillator model torsional spring: $\Delta G(\chi_{3,i}) = (\tau/2)(\chi_{3,i} - \chi_{3,0})^2$, where τ is the torsional spring force constant and $(\chi_{3,i} - \chi_{3,0})$ is the displacement from the equilibrium position.

structure coordinate. We model the side chain free energies about the equilibrium $\chi_{3,0}$ angles in terms of a simple Hooke's Law torsional model:

$$\Delta G(\chi_{3,i}) = \frac{\tau}{2}(\chi_{3,i} - \chi_{3,0})^2 \tag{10}$$

where τ is the torsional force constant. We can fit the free energy landscapes in Figure 11 to eq 10 to determine the torsional force constants along the χ_3 dihedral angle coordinate of Gln, Gln_3, and Asp_2-Gln_{10}-Lys_2. We find that $\tau \sim 12$ J·mol^{-1}·deg^{-2} for Gln, ~ 16 J·mol^{-1}·deg^{-2} for Gln_3, and ~ 13 J·mol^{-1}·deg^{-2} for Asp_2-Gln_{10}-Lys_2. The similarity of the Gln_3 and Asp_2-Gln_{10}-Lys_2 χ_3 angle torsional force constants of Gln most likely results from the similar side chain constraints and solvation states of these compounds.

CONCLUSIONS

We determined the dependence of the $AmIII^P$ band frequency on the χ_3 and χ_2 dihedral angles of Gln and Asn side chains. The $AmIII^P$ vibration is complex and consists of C_δ–N_ϵ (C_γ–N_δ) stretching and $N_\epsilon H_2$ ($N_\delta H_2$) rocking motions that are out-of-phase with C_β–C_γ (C_α–C_β) stretching in Gln (Asn). The frequency of the $AmIII^P$ vibration shows a cosinusoidal dependence on the χ_3 and χ_2 dihedral angles of the Gln and Asn side chains. The structural sensitivity of the $AmIII^P$ vibration derives from hyperconjugation between the C_β–C_γ (C_α–C_β) σ and the C_δ=O_ϵ (C_γ=O_δ) π^* orbitals. Hyperconjugation between these two orbitals increases the C_β–C_γ (C_α–C_β) bond length, which decreases the C_β–C_γ (C_α–C_β) stretching force constant and causes a downshift in the $AmIII^P$ frequency. In this case, hyperconjugation gives rise to spectroscopic markers diagnostic of local dihedral angles. This suggests that future studies of conformationally dependent hyperconjugation interactions will enable the discovery of new, structurally sensitive spectroscopic makers.

The correlations between the $AmIII^P$ frequency and the χ_3 and χ_2 dihedral angles of Gln and Asn side chains will be useful for protein conformational investigations, particularly for amyloid-like fibril and prion aggregates. In general, fibril and prion aggregates are insoluble and cannot be crystallized. Therefore, there are few approaches to obtain molecular-level structural information. As a result, little is known about the structure of Gln and Asn side chains in fibrils. The $AmIII^P$ spectroscopic marker band enables us to experimentally probe conformations of the Gln side chains of polyGln fibrils in order to obtain new, molecular-level insights into fibril structures.

ASSOCIATED CONTENT

Supporting Information

The Supporting Information is available free of charge on the ACS Publications website at DOI: 10.1021/acs.jpcb.5b07651.

Description of X-ray crystallographic methods to determine crystal structures, circular dichroism (CD) methodology (PDF)

MATLAB programs used to calculate PEDs from DFT calculations (ZIP)

L-glutamine *t*-butyl ester HCl (CIF)

AUTHOR INFORMATION

Corresponding Author

*E-mail: asher@pitt.edu.

Notes

The authors declare no competing financial interest.

ACKNOWLEDGMENTS

Funding for this work was provided by the University of Pittsburgh. E.M.D. gratefully acknowledges support through the NIH Molecular Biophysics and Structural Biology Training Grant (T32 GM88119). The computational work was supported by the University of Pittsburgh Center for Simulation and Modeling through the supercomputing resources provided. We thank Dr. Sergei V. Bykov for useful discussions and Prof. Roland Dunbrack, Jr., for providing his rotamer database.

REFERENCES

(1) Trottier, Y.; Lutz, Y.; Stevanin, G.; Imbert, G.; Devys, D.; Cancel, G.; Saudou, F.; Weber, C.; David, G.; Tora, L.; et al. Polyglutamine Expansion as a Pathological Epitope in Huntington's Disease and Four Dominant Cerebellar Ataxias. *Nature* **1995**, *378*, 403−406.

(2) Nance, M. A. Clinical Aspects of CAG Repeat Diseases. *Brain Pathol.* **1997**, *7*, 881−900.

(3) Ross, C. A.; Poirier, M. A. Protein Aggregation and Neurodegenerative Disease. *Nat. Med.* **2004**, *10*, S10−S17.

(4) Gatchel, J. R.; Zoghbi, H. Y. Diseases of Unstable Repeat Expansion: Mechanisms and Common Principles. *Nat. Rev. Genet.* **2005**, *6*, 743−755.

(5) Orr, H. T.; Zoghbi, H. Y. Trinucleotide Repeat Disorders. *Annu. Rev. Neurosci.* **2007**, *30*, 575−621.

(6) Wetzel, R. Physical Chemistry of Polyglutamine: Intriguing Tales of a Monotonous Sequence. *J. Mol. Biol.* **2012**, *421*, 466−90.

DOI: 10.1021/acs.jpcb.5b07651
J. Phys. Chem. B 2015, 119, 13039−13051

(7) Murphy, R. M.; Walters, R. H.; Tobelmann, M. D.; Bernacki, J. P. In *Non-fibrillar Amyloidogenic Protein Assemblies—Common Cytotoxins Underlying Degenerative Diseases*; Rahimi, F., Bitan, G., Eds.; Springer: Dordrecht, The Netherlands, 2012; Chapter 11, pp 337−375.
(8) Arrasate, M.; Finkbeiner, S. Protein Aggregates in Huntington's Disease. *Exp. Neurol.* **2012**, *238*, 1−11.
(9) Blum, E. S.; Schwendeman, A. R.; Shaham, S. PolyQ Disease: Misfiring of a Developmental Cell Death Program? *Trends Cell Biol.* **2013**, *23*, 168−174.
(10) Michelitsch, M. D.; Weissman, J. S. A Census of Glutamine/Asparagine-rich Regions: Implications for their Conserved Function and the Prediction of Novel Prions. *Proc. Natl. Acad. Sci. U. S. A.* **2000**, *97*, 11910−11915.
(11) Sivanandam, V. N.; Jayaraman, M.; Hoop, C. L.; Kodali, R.; Wetzel, R.; van der Wel, P. C. A. The Aggregation-Enhancing Huntingtin N-Terminus Is Helical in Amyloid Fibrils. *J. Am. Chem. Soc.* **2011**, *133*, 4558−4566.
(12) Schneider, R.; Schumacher, M. C.; Mueller, H.; Nand, D.; Klaukien, V.; Heise, H.; Riedel, D.; Wolf, G.; Behrmann, E.; Raunser, S.; et al. Structural Characterization of Polyglutamine Fibrils by Solid-State NMR Spectroscopy. *J. Mol. Biol.* **2011**, *412*, 121−136.
(13) Kar, K.; Hoop, C. L.; Drombosky, K. W.; Baker, M. A.; Kodali, R.; Arduini, I.; van der Wel, P. C.; Horne, W. S.; Wetzel, R. β-Hairpin-Mediated Nucleation of Polyglutamine Amyloid Formation. *J. Mol. Biol.* **2013**, *425*, 1183−1197.
(14) Sharma, D.; Shinchuk, L. M.; Inouye, H.; Wetzel, R.; Kirschner, D. A. Polyglutamine Homopolymers Having 8−45 Residues Form Slablike β-crystallite Assemblies. *Proteins: Struct., Funct., Genet.* **2005**, *61*, 398−411.
(15) Nelson, R.; Sawaya, M. R.; Balbirnie, M.; Madsen, A. O.; Riekel, C.; Grothe, R.; Eisenberg, D. Structure of the Cross-β Spine of Amyloid-like Fibrils. *Nature* **2005**, *435*, 773−778.
(16) Wiltzius, J. J. W.; Landau, M.; Nelson, R.; Sawaya, M. R.; Apostol, M. I.; Goldschmidt, L.; Soriaga, A. B.; Cascio, D.; Rajashankar, K.; Eisenberg, D. Molecular Mechanisms for Protein-Encoded Inheritance. *Nat. Struct. Mol. Biol.* **2009**, *16*, 973−8.
(17) Caswell, D. S.; Spiro, T. G. Ultraviolet Resonance Raman Spectroscopy of Imidazole, Histidine, and $Cu(Imidazole)_4^{2+}$: Implications for Protein Studies. *J. Am. Chem. Soc.* **1986**, *108*, 6470−6477.
(18) Miura, T.; Takeuchi, H.; Harada, I. Tryptophan Raman Bands Sensitive to Hydrogen Bonding and Side-chain Conformation. *J. Raman Spectrosc.* **1989**, *20*, 667−671.
(19) Harhay, G. P.; Hudson, B. S. Ultraviolet Resonance Raman Study of Proline Isomerization. *J. Phys. Chem.* **1991**, *95*, 3511−3513.
(20) Markham, L. M.; Mayne, L. C.; Hudson, B. S.; Zgierski, M. Z. Resonance Raman Studies of Imidazole, Imidazolium, and their Derivatives: the Effect of Deuterium Substitution. *J. Phys. Chem.* **1993**, *97*, 10319−10325.
(21) Maruyama, T.; Takeuchi, H. Effects of Hydrogen Bonding and Side-chain Conformation on the Raman bands of Tryptophan-2,4,5,6,7-d_5. *J. Raman Spectrosc.* **1995**, *26*, 319−324.
(22) Jordan, T.; Mukerji, I.; Wang, Y.; Spiro, T. G. UV Resonance Raman Spectroscopy and Hydrogen Bonding of the Proline Peptide Bond. *J. Mol. Struct.* **1996**, *379*, 51−64.
(23) Chi, Z.; Asher, S. A. UV Raman Determination of the Environment and Solvent Exposure of Tyr and Trp Residues. *J. Phys. Chem. B* **1998**, *102*, 9595−9602.
(24) Ahmed, Z.; Myshakina, N. S.; Asher, S. A. Dependence of the AmII'p Proline Raman Band on Peptide Conformation. *J. Phys. Chem. B* **2009**, *113*, 11252−11259.
(25) Takeuchi, H. Raman Spectral Marker of Tryptophan Conformation: Theoretical Basis and Extension to a Wider Range of Torsional Angle. *J. Mol. Struct.* **2012**, *1023*, 143−148.
(26) Oladepo, S. A.; Xiong, K.; Hong, Z.; Asher, S. A.; Handen, J.; Lednev, I. K. UV Resonance Raman Investigations of Peptide and Protein Structure and Dynamics. *Chem. Rev.* **2012**, *112*, 2604−2628.
(27) Hong, Z.; Wert, J.; Asher, S. A. UV Resonance Raman and DFT Studies of Arginine Side Chains in Peptides: Insights into Arginine Hydration. *J. Phys. Chem. B* **2013**, *117*, 7145−7156.
(28) Punihaole, D.; Jakubek, R. S.; Dahlburg, E. M.; Hong, Z.; Myshakina, N. S.; Geib, S.; Asher, S. A. UV Resonance Raman Investigation of the Aqueous Solvation Dependence of Primary Amide Vibrations. *J. Phys. Chem. B* **2015**, *119*, 3931−3939.
(29) Dudik, J. M.; Johnson, C. R.; Asher, S. A. UV Resonance Raman Studies of Acetone, Acetamide, and N-Methylacetamide: Models for the Peptide Bond. *J. Phys. Chem.* **1985**, *89*, 3805−3814.
(30) Xiong, K.; Punihaole, D.; Asher, S. A. UV Resonance Raman Spectroscopy Monitors Polyglutamine Backbone and Side Chain Hydrogen Bonding and Fibrillization. *Biochemistry* **2012**, *51*, 5822−5830.
(31) Wang, Y.; Purrello, R.; Georgiou, S.; Spiro, T. G. UVRR Spectroscopy of the Peptide Bond. 2. Carbonyl H-Bond Effects on the Ground- and Excited-State Structures of N-methylacetamide. *J. Am. Chem. Soc.* **1991**, *113*, 6368−6377.
(32) Triggs, N. E.; Valentini, J. J. An Investigation of Hydrogen Bonding in Amides Using Raman Spectroscopy. *J. Phys. Chem.* **1992**, *96*, 6922−6931.
(33) Markham, L. M.; Hudson, B. S. Ab Initio Analysis of the Effects of Aqueous Solvation on the Resonance Raman Intensities of N-Methylacetamide. *J. Phys. Chem.* **1996**, *100*, 2731−2737.
(34) Myshakina, N. S.; Ahmed, Z.; Asher, S. A. Dependence of Amide Vibrations on Hydrogen Bonding. *J. Phys. Chem. B* **2008**, *112*, 11873−11877.
(35) Asher, S. A.; Ianoul, A.; Mix, G.; Boyden, M. N.; Karnoup, A.; Diem, M.; Schweitzer-Stenner, R. Dihedral ψ Angle Dependence of the Amide III Vibration: A Uniquely Sensitive UV Resonance Raman Secondary Structural Probe. *J. Am. Chem. Soc.* **2001**, *123*, 11775−11781.
(36) Asher, S. A.; Mikhonin, A. V.; Bykov, S. UV Raman Demonstrates that α-Helical Polyalanine Peptides Melt to Polyproline II Conformations. *J. Am. Chem. Soc.* **2004**, *126*, 8433−8440.
(37) Mikhonin, A. V.; Bykov, S. V.; Myshakina, N. S.; Asher, S. A. Peptide Secondary Structure Folding Reaction Coordinate: Correlation Between UV Raman Amide III Frequency, Ψ Ramachandran Angle, and Hydrogen Bonding. *J. Phys. Chem. B* **2006**, *110*, 1928−1943.
(38) Mikhonin, A. V.; Asher, S. A. Direct UV Raman Monitoring of 3_{10}-Helix and π-Bulge Premelting During α-Helix Unfolding. *J. Am. Chem. Soc.* **2006**, *128*, 13789−13795.
(39) Ma, L.; Ahmed, Z.; Mikhonin, A. V.; Asher, S. A. UV Resonance Raman Measurements of Poly-L-Lysine's Conformational Energy Landscapes: Dependence on Perchlorate Concentration and Temperature. *J. Phys. Chem. B* **2007**, *111*, 7675−7680.
(40) Xiong, K.; Asciutto, E. K.; Madura, J. D.; Asher, S. A. Salt Dependence of an α-Helical Peptide Folding Energy Landscapes. *Biochemistry* **2009**, *48*, 10818−10826.
(41) Xiong, K.; Asher, S. A. Circular Dichroism and UV Resonance Raman Study of the Impact of Alcohols on the Gibbs Free Energy Landscape of an α-Helical Peptide. *Biochemistry* **2010**, *49*, 3336−3342.
(42) Ma, L.; Hong, Z.; Sharma, B.; Asher, S. A. UV Resonance Raman Studies of the $NaClO_4$ Dependence of Poly-L-lysine Conformation and Hydrogen Exchange Kinetics. *J. Phys. Chem. B* **2012**, *116*, 1134−1142.
(43) Hong, Z.; Damodaran, K.; Asher, S. A. Sodium Dodecyl Sulfate Monomers Induce XAO Peptide Polyproline II to α-Helix Transition. *J. Phys. Chem. B* **2014**, *118*, 10565−10575.
(44) Shapovalov, M.; Dunbrack, R. L. A Smoothed Backbone-Dependent Rotamer Library for Proteins Derived from Adaptive Kernel Density Estimates and Regressions. *Structure* **2011**, *19*, 844−858.
(45) Shimanouchi, T. *Tables of Molecular Vibrational Frequencies Consolidated Volume I*; National Bureau of Standards: Gaithersburg, MD, 1972.
(46) Asher, S. A.; Bormett, R. W.; Chen, X. G.; Lemmon, D. H.; Cho, N.; Peterson, P.; Arrigoni, M.; Spinelli, L.; Cannon, J. UV Resonance Raman Spectroscopy Using a New CW Laser Source: Convenience and Experimental Simplicity. *Appl. Spectrosc.* **1993**, *47*, 628−633.

DOI: 10.1021/acs.jpcb.5b07651
J. Phys. Chem. B 2015, 119, 13039−13051

(47) Bykov, S.; Lednev, I.; Ianoul, A.; Mikhonin, A.; Munro, C.; Asher, S. A. Steady-State and Transient Ultraviolet Resonance Raman Spectrometer for the 193−270 nm Spectral Region. *Appl. Spectrosc.* **2005**, *59*, 1541−1552.
(48) Kohn, W.; Sham, L. J. Self-Consistent Equations Including Exchange and Correlation Effects. *Phys. Rev.* **1965**, *140*, A1133−A1138.
(49) Frisch, M. J.; Trucks, G. W.; Schlegel, H. B.; Scuseria, G. E.; Robb, M. A.; Cheeseman, J. R.; Scalmani, G.; Barone, V.; Mennucci, B.; Petersson, G. A. et al. *Gaussian09*, revision D.01; Gaussian Inc.: Wallingford, CT, 2009.
(50) Zhao, Y.; Truhlar, D. The M06 Suite of Density Functionals for Main Group Thermochemistry, Thermochemical Kinetics, Noncovalent Interactions, Excited States, and Transition Elements: Two New Functionals and Systematic Testing of Four M06-class Functionals and 12 Other Functionals. *Theor. Chem. Acc.* **2008**, *120*, 215−241.
(51) Dhamelincourt, P.; Ramirez, F. Polarized Micro-Raman and FT-IR Spectra of L-Glutamine. *Appl. Spectrosc.* **1993**, *47*, 446−451.
(52) Ramírez, F. J.; Tuñón, I.; Silla, E. Amino Acid Chemistry in Solution: Structural Study and Vibrational Dynamics of Glutamine in Solution. An ab Initio Reaction Field Model. *J. Phys. Chem. B* **1998**, *102*, 6290−6298.
(53) Clark, L. B. Polarization Assignments in the Vacuum UV Spectra of the Primary Amide, Carboxyl, and Peptide Groups. *J. Am. Chem. Soc.* **1995**, *117*, 7974−7986.
(54) Bohlmann, F. Zur Konfigurationsbestimmung von Chinolizin-Derivaten. *Angew. Chem.* **1957**, *69*, 641−642.
(55) Lii, J.-H.; Chen, K.-H.; Allinger, N. L. Alcohols, Ethers, Carbohydrates, and Related Compounds Part V. The Bohlmann Torsional Effect. *J. Phys. Chem. A* **2004**, *108*, 3006−3015.
(56) Bykov, S. V.; Myshakina, N. S.; Asher, S. A. Dependence of Glycine CH_2 Stretching Frequencies on Conformation, Ionization State, and Hydrogen Bonding. *J. Phys. Chem. B* **2008**, *112*, 5803−5812.
(57) Adhikary, R.; Zimmermann, J.; Liu, J.; Forrest, R. P.; Janicki, T. D.; Dawson, P. E.; Corcelli, S. A.; Romesberg, F. E. Evidence of an Unusual N-H N Hydrogen Bond in Proteins. *J. Am. Chem. Soc.* **2014**, *136*, 13474−13477.
(58) Rhys, N. H.; Soper, A. K.; Dougan, L. The Hydrogen-Bonding Ability of the Amino Acid Glutamine Revealed by Neutron Diffraction Experiments. *J. Phys. Chem. B* **2012**, *116*, 13308−13319.
(59) Cochran, W.; Penfold, B. R. The Crystal Structure of L-Glutamine. *Acta Crystallogr.* **1952**, *5*, 644−653.
(60) Mikhonin, A. V.; Myshakina, N. S.; Bykov, S. V.; Asher, S. A. UV Resonance Raman Determination of Polyproline II, Extended 2.5_1-helix, and β-sheet Ψ Angle Energy Landscape in Poly-L-Lysine and Poly-L-Glutamic Acid. *J. Am. Chem. Soc.* **2005**, *127*, 7712−20.
(61) Richardson, J. S. *The Anatomy and Taxonomy of Protein Structure*; Academic Press: New York, 1981; Vol. *34*.
(62) Hollingsworth, S. A.; Berkholz, D. S.; Karplus, P. A. On the Occurrence of Linear Groups in Proteins. *Protein Sci.* **2009**, *18*, 1321−1325.
(63) Chen, S.; Wetzel, R. Solubilization and Disaggregation of Polyglutamine Peptides. *Protein Sci.* **2001**, *10*, 887−891.
(64) Chellgren, B. W.; Miller, A.; Creamer, T. P. Evidence for Polyproline II Helical Structure in Short Polyglutamine Tracts. *J. Mol. Biol.* **2006**, *361*, 362−371.

DOI: 10.1021/acs.jpcb.5b07651
J. Phys. Chem. B 2015, 119, 13039−13051